

Variational Osmosis for Non-linear Image Fusion

Simone Parisotto, Luca Calatroni, Aurelie Bugeau, Nicolas Papadakis and Carola-Bibiane Schönlieb.

Abstract—We propose a new variational model for nonlinear image fusion. Our approach incorporates the osmosis model proposed in Vogel et al. (2013) and Weickert et al. (2013) as an energy term in a variational model. The osmosis energy is known to realize visually plausible image data fusion. As a consequence, our method is invariant to multiplicative brightness changes. On the practical side, it requires minimal supervision and parameter tuning and can encode prior information on the structure of the images to be fused. We develop a primal-dual algorithm for solving this new image fusion model and we apply the resulting minimisation scheme to multi-modal image fusion for face fusion, colour transfer and some cultural heritage conservation challenges. Visual comparison to state-of-the-art proves the quality and flexibility of our method.

Index Terms—Osmosis filtering, image fusion, non-convex optimisation, primal-dual algorithm, cultural heritage imaging.

I. INTRODUCTION

Image fusion is broadly referred to as the problem of gluing information from two (or more) images so as to create a composite image, with new structures and/or enhanced details. A recent survey [17] has shown the increasing interest for image fusion for a wide range applications. Image fusion can be used for image editing [29], image enhancement [3] focus-stacking imaging [18], HDR imaging [22], dehazing [2], facial texture transfers [31], etc. Moreover, image fusion can be used as a technique to unveil hidden information visible only by means of multi-modal image modalities, see, e.g. [8], [28] and its applications to cultural heritage. In the context of medical imaging, image fusion enables to combine different modalities for better diagnosis [16]. Combining multiple modalities (e.g. in photography, visible light from a standard camera sensor with spectral imaging bands such as infrared) is also useful for video surveillance or remote sensing [21].

As highlighted in [23], image fusion started with simple spatial domain techniques such as averaging or principal component analysis. Almost all classical approaches now involve multiscale decomposition techniques in spatial or spectral domain, such as, for instance, wavelet [26] and Laplacian pyramid decomposition [6], see also [1] for a review.

Over the last twenty years, mathematical models for image fusion based on the use of variational techniques and first and second order PDEs have also been considered. A very popular variational model is the well-known Poisson image editing [29]. The (unknown) fused image is computed by minimising

the difference between its gradient and the one of the plain gluing of the two images to be fused in a subregion of the image domain. Equivalently, the Poisson editing problem, can be formulated in terms of a linear elliptic PDE, endowed with appropriate boundary conditions. In terms of evolution models, a linear isotropic drift-diffusion PDE describing the physical phenomenon of osmosis [15] has been proposed in [33] to solve the image fusion problem. Compared to the standard Poisson editing model, the main advantage of the linear osmosis model is its invariance to multiplicative brightness changes, which makes the fusion much more effective in the presence of images with different contrast. Furthermore, the image osmosis model shows high flexibility when applied to other type of problems such as image compression and shadow removal, and is amenable for efficient numerical schemes guaranteeing mass and positivity preservation of the solution, see [7], [32]. In order to overcome the Laplace smoothing of the osmosis model when applied to this latter problem, recently, an anisotropic variant of the osmosis model driving image diffusion along coherent directions has been considered in [27]. In this model the two different steps, reference drift estimation and image reconstruction, are performed in a disjoint way.

The use of nonlinear models for image fusion has recently been proposed in [5], where the nonlinear spectral decomposition of the Total Variation (TV) regularisation functional is used to improve texture details fusion in a multiscale scheme. The good performance of such approach is, however, somehow limited by the manual pre-processing (e.g. an image alignment step) and careful parameter choice (such as the choice of specific eigenvectors extracted from both images capturing fine details with sufficient precision) required.

Contribution: We propose a novel nonlinear image fusion approach based on a variational model. We show that our method improves upon the aforementioned drawbacks both of the osmosis model and of the spectral methods. Our model requires little supervision and parameter tuning by performing jointly the estimation of the image corresponding to the drift (driving the osmosis regularisation) and the corresponding reconstruction. It enhances chromatic consistency with the image to-be-fused and favours better texture preservation at the same time, see Figure 1.

With the proposed variational model we obtain a fused image u from two given foreground and background images, respectively denoted by f and b , whose structures are forced to be glued together by a dedicated image v via a mixing α -map. The solution of the model is computed as a minimising pair (u, v) of the energy functional

$$\min_{u,v} \mathcal{E}(u, v) := \mathcal{O}(u, v) + \gamma \mathcal{D}(u) + \eta \mathcal{R}(v), \quad (1)$$

S. Parisotto and C.-B. Schönlieb are with DAMTP, University of Cambridge, Cambridge CB3 0WA, UK. Correspondence e-mail: sp751@cam.ac.uk

L. Calatroni is with CNRS, Université Côte d'Azur, INRIA, I3S, UMR 7271, Sophia-Antipolis, France

A. Bugeau is with Univ. Bordeaux, Bordeaux INP, CNRS, LaBRI, UMR 5800, F-33400 Talence, France

N. Papadakis is with CNRS, Univ. Bordeaux, IMB, UMR 5251, F-33400 Talence, France

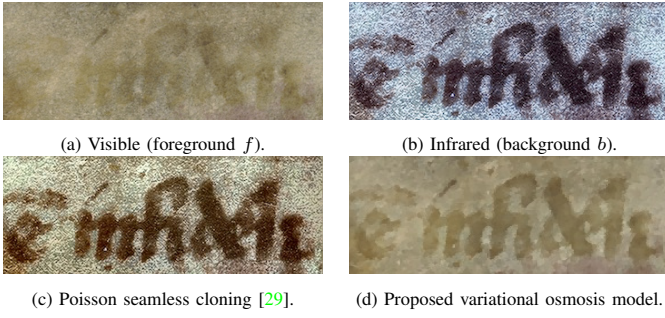


Figure 1: Multi-modal fusion for Cultural Heritage images. The structures of the infrared image (b) are transferred to the visible one (a). Structural regularisation and chromatic preservation is tangible in our nonlinear model (d), with $\alpha = 0.5$ everywhere, compared to the linear seamless cloning [29] shown in (c).

where \mathcal{O} denotes an *osmosis*-based term promoting image fusion, \mathcal{D} is a fidelity term forcing u to stay close to f in the foreground region and \mathcal{R} acts as a regulariser enhancing the salient information of the structural image v . These terms are weighted with non negative parameters γ and η and detailed in Section III.

Our model allows for more flexibility than [5] as it can take into account possible prior information available on the structures to-be-fused (such as, for instance piece-wise constant images) encoded in v . We use non-convex optimisation algorithms for computing efficiently a numerical solution of the problem. Numerical results show that the proposed model outperforms state-of-the-art linear and nonlinear methods for several face fusion, colour transfer and heritage imaging applications in terms of chromaticity errors and texture preservation.

Organisation of the paper: this paper is organised as follows. In Section II we review some classical methods for image fusion based on the formulation of the problem in a variational and a Partial Differential Equation (PDE) form, highlighting their limitations mainly in terms of over-smoothing and misalignment artefacts. In Section III we introduce the variational osmosis model and discuss on its analytical interpretation. In Section IV we describe the details needed for the computation of the numerical solution of the proposed model, which is used in Section V for fusing data in a variety of applications involving image fusion (such as face fusion and multi-modal fusion from data acquired in Cultural Heritage conservation contexts).

II. VARIATIONAL AND PDE MODELS FOR IMAGE FUSION

This section presents related models for image fusion.

Poisson editing: A very simple and classical model for image fusion is the Poisson editing model proposed by Pérez et al. in [29]. The model aims at fusing areas of two different images in a visually plausible way. In detail, given two colour images f and b defined on the same image domain Ω , the model copies a (not necessarily connected) sub-region $A \subset \Omega \subset \mathbb{R}^2$ of f over b by means of a guidance field d .

When $d = \nabla v$ is the gradient of a source function v , and taking $v = f$ as in [29], the model can be mathematically expressed channel-wise in the following variational form:

$$\text{find } u^* \text{ s.t. } u^* \in \arg \min_u \int_A |\nabla u(\mathbf{x}) - \nabla v(\mathbf{x})|^2 d\mathbf{x}, \quad (2)$$

coupled with suitable constraints for instance of the form:

$$u_{\Omega \setminus A} = b_{\Omega \setminus A}, \quad (3)$$

so as to force the matching of the resulting image u^* with b outside A , while driving the fusion inside A using the structural information coming from f . Note that in the original formulation of the Poisson editing problem, the condition (3) is imposed only on ∂A as a boundary condition for the corresponding PDE. However, we extend here the constraint to draw more connections with our proposed model, as it will be clear in the following. Note that the problem above can be formulated over the whole domain Ω as:

$$\text{find } u^* \text{ s.t. } u^* \in \arg \min_u \int_{\Omega} \chi_A(\mathbf{x}) |\nabla u(\mathbf{x}) - \nabla v(\mathbf{x})|^2 d\mathbf{x},$$

coupled with (3), where χ_A is the characteristic function of the subset A defined by:

$$\chi_A(\mathbf{x}) := \begin{cases} 0 & \text{if } \mathbf{x} \notin A \\ 1 & \text{if } \mathbf{x} \in A. \end{cases} \quad (4)$$

By computing the correspondent Euler-Lagrange equation, the model can be equivalently rewritten by means of a linear elliptic Poisson PDE, so as to solve:

$$\text{find } u^* \text{ s.t. } \Delta u^* = \Delta v \text{ on } A,$$

coupled with (3). The solution u^* of the problem above is indeed the steady state of the parabolic Poisson editing PDE

$$\partial_t u = \text{div}(\chi_A(\nabla u - \nabla v)), \quad \text{on } \Omega,$$

which corresponds to the steepest descent formulation of the variational problem defined on the whole Ω .

This simple model has been used for several seamless cloning applications, such as image insertion or feature exchange. Poisson editing falls into the category of gradient domain methods (see also [12]) and shares with them the capability of recovering v inside A up to an additive constant. This property of gradient domain methods constitutes one of its main limitations when applied for instance to the problem of image cloning. By allowing for any colour channel only additive value shifts, Poisson editing is not able to fuse a low contrast image into a high contrast one, see Figure 4b.

Image osmosis: A more flexible model allowing for multiplicative image variations and applicable to many more problems (shadow removal, image decompression and many more) is the parabolic image osmosis model originally proposed in [33] and later considered in few other works, e.g. [7], [27], [32]. Given a final stopping time $T > 0$, two positive images $u^0, v : \Omega \rightarrow \mathbb{R}_+$, a so called *drift* vector field defined as

$$d := \nabla \log v \quad (5)$$

and a positive definite symmetric matrix field $\mathbf{W} : \Omega \rightarrow \mathbb{R}^2$, the general, possibly anisotropic, convection-diffusion PDE osmosis model reads:

$$\begin{cases} u_t = \operatorname{div}(\mathbf{W}(\nabla u - \mathbf{d}u)) & \text{on } \Omega \times (0, T], \\ u(\mathbf{x}, 0) = u^0(\mathbf{x}) & \text{on } \Omega, \\ \langle \mathbf{W}(\nabla u - \mathbf{d}u), \mathbf{n} \rangle = 0 & \text{on } \partial\Omega \times (0, T], \end{cases} \quad (6)$$

where \mathbf{n} denotes the outer normal vector on $\partial\Omega$.

In [15], [33], the authors looked at the statistical interpretation and at the theoretical foundation of the model in its isotropic form, i.e. where $\mathbf{W} = \mathbf{I}$, the 2×2 identity matrix, also providing in [32] a fully-discrete theory for its consistent and efficient numerical realisation. In [11], Dirichlet and mixed boundary conditions have been also studied for the linear osmosis model. In the case of standard Neumann b.c. and when $\mathbf{W} \neq \mathbf{I}$, the diffusivity tensor is non-constant and favours anisotropic diffusion and transport, making it amenable for directional image completion, i.e. inpainting, see [27].

Solutions to (6) enjoy non-negativity and mass conservation properties. The main difference with standard diffusion models is their convergence to a non-constant steady state u^* which turns out to be a rescaled version of the given image v in terms of the average of the ratio between the mean of u^0 and v , that is

$$u^*(\mathbf{x}) = \frac{\mu_{u^0}}{\mu_v} v(\mathbf{x}), \quad \mathbf{x} \in \Omega,$$

where for any integrable function $g : \Omega \rightarrow \mathbb{R}$ we set $\mu_g := \frac{1}{|\Omega|} \int_{\Omega} g(\mathbf{x}) \, d\mathbf{x}$, which has to be understood channel-wise.

Model (6) also has a variational counterpart, where the multiplicative nature of osmosis appears explicitly: its steady state is the solution of the Euler-Lagrange equation of the functional E defined by:

$$\begin{aligned} E(u) &= \int_{\Omega} v(\mathbf{x}) \nabla^{\top} \left(\frac{u(\mathbf{x})}{v(\mathbf{x})} \right) \mathbf{W}(\mathbf{x}) \nabla \left(\frac{u(\mathbf{x})}{v(\mathbf{x})} \right) \, d\mathbf{x} \\ &= \int_{\Omega} v(\mathbf{x}) \left\| \nabla \left(\frac{u(\mathbf{x})}{v(\mathbf{x})} \right) \right\|_{\mathbf{W}}^2 \, d\mathbf{x}, \end{aligned} \quad (7)$$

where $\|e\|_{\mathbf{W}} := \sqrt{\langle e, \mathbf{W}e \rangle}$ is the scalar product weighted by the matrix \mathbf{W} , see [27, Proposition 2.3].

The image osmosis model has been shown to be very flexible for a variety of image processing tasks, e.g. image compression [33], artefact-free shadow removal [7], [27], contrast equalisation and multi-modal image fusion in particular in the context of Cultural Heritage imaging [8], [28].

From a numerical point of view, explicit, implicit [32], and semi-implicit schemes based on the dimensional decomposition of the space-discretisation operators [7] have been considered for the efficient computation of the solution of the isotropic model. In [27], suitable anisotropic stencils and efficient time-integration schemes have been introduced to further provide a discrete theory for the anisotropic case, exploiting ideas of Lattice Basis Reduction (LBR) models proposed in [13] for pure diffusion processes and adapted to deal with the convection part as well. For all these schemes, the discrete conservation of mass and non-negativity properties,

along with convergence results, were proved. The generic time stepping scheme takes the form:

$$\mathbf{u}_{k+1} = \mathbf{P}\mathbf{u}_k, \quad k \geq 1, \quad (8)$$

for $\mathbf{u}^0 \in \mathbb{R}_+^S$ being the discretised version of $u^0(\mathbf{x})$. Note that in [27] the anisotropic tensor \mathbf{W} (6) is computed with respect to the given image u^0 only, thus making the model linear. Local coherence direction estimation is performed in [27] in terms of the multi-scale tensor voting technique proposed in [24] to make structure tensor approaches more robust.

Nonlinear models: Nonlinear models for image fusion has recently been considered in [5]. They are based on the computation of the (suitably defined) spectral decomposition of one-homogeneous functionals (such as the Total Variation semi-norm) and on their use as a basis capturing multi-scale (texture) details. Such property is indeed exploited in [5] to deal also with related imaging problems such as image insertion and artistic image transformation. One of the main drawbacks of this approach is the precise (and often heuristic) selection of the eigenvectors extracted from the images to fuse required to combine information with enough precision. Moreover, the pre-processing steps require a fine tuning of the relevant features to be glued. Finally, in the case of face fusion, the somatic features are required to be perfectly aligned.

Starting from these preliminary studies, we propose to codify the osmosis idea within the formulation of a new variational image regulariser adapted to solve a great variety of image fusion problems.

III. A JOINT OSMOSIS-RECONSTRUCTION MODEL

We now present the osmosis-driven fusion term and the joint variational osmosis model to smoothly fuse together a foreground image f and background image b .

In order to favour the fusion process at the boundary of the foreground image $A \subset \Omega$, we will use in the following the notion of α -map associated to A , defined essentially as the indicator function of A which takes the value 1/2 on the boundary ∂A . However, for some of the applications considered in the following, we will consider a smoother notion, by which the α -map is defined as the convolution of the indicator function χ_A in (4) with a compactly supported kernel $\omega \in C_c^\infty(\Omega)$, that is:

$$\alpha(\mathbf{x}) := (\omega * \chi_A)(\mathbf{x}), \quad \mathbf{x} \in \Omega, \quad (9)$$

where $*$ stands for the convolution operation. Under such definition, the transition from 0 to 1 is thus made smoother on ∂A . In this work we use the same terminology to indicate both cases, see Section V and Figure 2 for some examples.

In the following section, we will make precise the three terms appearing in model (1).

A. Osmosis-driven fusion term

We denote by u the image to estimate which shall smoothly fuse the information contained in f and b . We model such fusion using the osmosis variational energy in (7), which is defined in terms of an additional image v which has to be

estimated. The idea here is to use as v an image whose associated drift $\nabla \log v$ is related to the structural information contained both in f and in b . For every $\mathbf{x} \in \Omega$, a possible choice for that consists in choosing the reference drift as:

$$\tilde{\mathbf{d}}(\mathbf{x}) = \nabla \log \left(f(\mathbf{x})^{\alpha(\mathbf{x})} b(\mathbf{x})^{1-\alpha(\mathbf{x})} \right). \quad (10)$$

Note that in the case of a scalar α -map (i.e. when $\alpha(\mathbf{x}) \equiv \alpha \in [0, 1]$) and by simple algebraic manipulations, this choice for $\tilde{\mathbf{d}}$ is nothing but the convex combination of the drifts associated to f and b , respectively. In order to enforce v to stay locally close to such reference image $f^\alpha b^{1-\alpha}$, we thus incorporate in our model a natural penalisation term, weighted by a parameter $\mu > 0$. Combining altogether, the proposed osmosis-driven fusion term, depending both on u and v , thus reads

$$\mathcal{O}(u, v) = \frac{1}{2} \int_{\Omega} v(\mathbf{x}) \left| \nabla \left(\frac{u(\mathbf{x})}{v(\mathbf{x})} \right) \right|^2 d\mathbf{x} + \frac{\mu}{2} \|v - f^\alpha b^{1-\alpha}\|_2^2. \quad (11)$$

This non-convex term combines the osmosis term (7) with a quadratic term which acts as a fidelity term for v enforcing locally the consistency with both f and b . Note that compared to (7), in the first term above we set $\mathbf{W} = \mathbf{I}$, making the osmosis energy purely isotropic since in this work we are not interested in encoding spatially varying directions for interpolation purposes as in [27].

B. Data fidelity and regularisation

We combine the osmosis-driven term (11) with two further terms. The first one acts as a fidelity term imposing u to stay close to f in the foreground region (i.e. for every $\mathbf{x} \in \Omega$ s.t. $\alpha(\mathbf{x}) > 0$):

$$\mathcal{D}(u) = \frac{1}{2} \int_{\Omega} \alpha(\mathbf{x}) (u(\mathbf{x}) - f(\mathbf{x}))^2 d\mathbf{x}. \quad (12)$$

We remark that although the L^2 term appearing in (11) clearly plays the role of a data fidelity on v and could be consequently combined with the term in (12), we nonetheless decided to leave it in the definition of the osmosis term \mathcal{O} to underline the importance of its closeness to the image $f^\alpha b^{1-\alpha}$ to favour the osmosis-driven regularisation. The numerical schemes we will consider in the following therefore respect such a decomposition.

As we are going to show in our following numerical experiments, for many real-world applications the combination of these two terms seems already to produce satisfying results. However, whenever prior information is available on the image v , the model can even be improved by introducing a further regularisation term acting on v which will be denoted by $\mathcal{R}(v)$. We consider in this paper the L^1 norm of the image gradient to promote gradient sparsity

$$\mathcal{R}(v) = \int_{\Omega} |\nabla u(\mathbf{x})| d\mathbf{x}.$$

This results into a piece-wise fusion of the image information, in contrast to the smoothing introduced by the α -map, so as to fuse only the relevant features from the foreground f and background b , e.g. in text fusion applications as in Figure 7.

These three terms are merged in the final proposed model (1). By varying the weights μ in (11), and γ and η in our model (1), recalled here for better readability

$$\min_{u, v} \mathcal{E}(u, v) := \mathcal{O}(u, v) + \gamma \mathcal{D}(u) + \eta \mathcal{R}(v),$$

we observe different behaviour on the final images depending also on the initial condition considered. As one can easily grasp, this is due to the non-convexity of the joint model whose careful analytical study guaranteeing also the existence of local minimisers is left for future research. Empirical considerations on these aspects are discussed in Section V.

IV. NUMERICAL SOLUTION

The energy in (1) is composed of three terms: the osmosis-driven term $\mathcal{O}(u, v)$ in (11), coupling in a non-convex way two smooth terms, the convex and smooth data term $\mathcal{D}(u)$ (12) and a regularisation function $\mathcal{R}(v)$ that could be either smooth (e.g. Tikhonov-type) or non-smooth (e.g. the L^1 norm of the gradient).

In order to exploit the structure of these coupled terms so as to compute a local minima of problem (1), we can apply the iPiano algorithm [25]. The corresponding iterative scheme reads for $k \geq 0$

$$\begin{cases} u^{k+1} = \mathbf{prox}_{\zeta_1^k \gamma \mathcal{D}}(u^k - \zeta_1^k \partial_u \mathcal{O}(u^k, v^k) + \beta_1(u^k - u^{k-1})), \\ v^{k+1} = \mathbf{prox}_{\zeta_2^k \eta \mathcal{R}}(v^k - \zeta_2^k \partial_v \mathcal{O}(u^k, v^k) + \beta_2(v^k - v^{k-1})), \end{cases} \quad (13)$$

for some initial guesses u^0, v^0 , positive inertial scalar steps β_1, β_2 and time-step sequences ζ_1^k, ζ_2^k , computed via backtracking in terms of the Lipschitz constant estimates $L_{1,k}, L_{2,k}$ of $\partial_u \mathcal{O}(u, v)$ and $\partial_v \mathcal{O}(u, v)$, respectively, via

$$\zeta_1^k < 2(1 - \beta_1)/L_{1,k} \quad \text{and} \quad \zeta_2^k < 2(1 - \beta_2)/L_{2,k}$$

s.t. $L_{1,k} \in \{L_{1,k-1}, \lambda L_{1,k-1}, \lambda^2 L_{1,k-1}, \dots\}$ is minimal satisfying

$$\begin{aligned} \mathcal{O}(u^{k+1}, v) &\leq \mathcal{O}(u^k, v) + \langle \partial_u \mathcal{O}(u^k, v), u^{k+1} - u^k \rangle \\ &\quad + \frac{L_{1,k}}{2} \|u^{k+1} - u^k\|_2^2, \end{aligned}$$

and the same holds for $L_{2,k}$.

The algorithm requires the computation of the derivative of the smooth term $\mathcal{O}(u, v)$ and the proximal operators of the two other terms. We now detail these computations, while the whole process is presented in Algorithm 1.

1) *Derivatives of $\mathcal{O}(u, v)$* : The gradient of with respect of the variable u is first obtained as

$$\begin{aligned} \partial_u \mathcal{O}(u, v) &= -\frac{1}{v} \operatorname{div} \left(v \left(\frac{\nabla u}{v} - \frac{u \nabla v}{v^2} \right) \right) \\ &= -\frac{(\Delta u - \operatorname{div}(\mathbf{d}u))}{v} \end{aligned} \quad (14)$$

where $\mathbf{d} := \nabla \log v$, $\nabla^* = -\operatorname{div}$, $\nabla^* \nabla = -\Delta$ and where we assumed Neumann boundary conditions $\langle \nabla u - \mathbf{d}u, \mathbf{n} \rangle = 0$. The gradient with respect to v is (see Appendix A):

$$\begin{aligned} \partial_v \mathcal{O}(u, v) &= -\frac{1}{2v^2} |\nabla u|^2 + \frac{2u}{v^3} \nabla u \cdot \nabla v + \operatorname{div} \left(\frac{u}{v^2} \cdot \nabla u \right) \\ &\quad - \frac{3u^2}{2v^4} |\nabla v|^2 - 2v \operatorname{div} \left(\frac{u^2}{v^3} \nabla v \right) \\ &\quad + \mu(v - f^\alpha b^{1-\alpha}). \end{aligned} \quad (15)$$

2) *Proximal operator of $\mathcal{D}(u)$* : The proximal step is simply

$$\begin{aligned} \mathbf{prox}_{\zeta_1^k \gamma \mathcal{D}}(u_\diamond^k) &= \arg \min_u \frac{\gamma}{2} \|\sqrt{\alpha}(u - f)\|_2^2 + \frac{1}{2\zeta_1^k} \|u - u_\diamond^k\|_2^2 \\ &= \left(\gamma\alpha + \frac{1}{\zeta_1^k} \right)^{-1} \left(\gamma\alpha f + \frac{1}{\zeta_1^k} u_\diamond^k \right). \end{aligned} \quad (16)$$

3) *Proximal operator of $\mathcal{R}(v)$* : If \mathcal{R} is smooth (for instance, if Tikhonov regularisation $\mathcal{R}(v) = \frac{1}{2} \|\nabla v\|^2$ is used), explicit gradient descent can be performed instead of computing an implicit proximal point. The current step can thus be integrated with $\partial_v \mathcal{O}$ so that the full update on v in (13) becomes:

$$v^{k+1} = v^k - \zeta_2^k (\partial_v \mathcal{O}(u^k, v^k) + \partial_v \mathcal{R}(v^k)) + \beta_2 (v^k - v^{k-1}).$$

However, implicit schemes need to be considered when \mathcal{R} is not smooth, e.g. for Total Variation-like regularisers. A standard way-around to improve the computational efficiency for such calculation consists in substituting the L^1 term with its Huber regularisation \mathcal{H}_ε depending on a small parameter $0 < \varepsilon \ll 1$, see, e.g., [9] for details. This promotes quadratic regularisation for homogeneous areas where $\|\nabla v\|_1 \leq \varepsilon$, and L^1 gradient regularisation wherever the $\|\nabla v\|_1 > \varepsilon$. The proximal step for the Huberised TV is computed by solving the problem

$$\mathbf{prox}_{\zeta_2^k \eta \mathcal{H}_\varepsilon}(v_\diamond^k) = \arg \min_v \eta \mathcal{H}_\varepsilon(\nabla v) + \frac{1}{2\zeta_2^k} \|v - v_\diamond^k\|_2^2. \quad (17)$$

Following [9], we can reformulate (17) as the following saddle point problem¹

$$\min_p \max_{\mathbf{y}} \underbrace{-\mathcal{H}_\varepsilon^*(\mathbf{y}) + \langle \nabla p, \mathbf{y} \rangle + \frac{1}{2\zeta_2^k} \|p - v_\diamond^k\|_2^2}_{s(p)}. \quad (18)$$

where, with a little abuse of notation, we have defined $\mathcal{H}_\varepsilon^*(\mathbf{y}) := (\eta \mathcal{H}_\varepsilon)^*(\mathbf{y}) = \frac{\varepsilon}{2\eta} \|\mathbf{y}\|^2 + \delta_{\|\cdot\|_{2,\infty} \leq \eta}(\mathbf{y})$. Since $s(p)$ is strongly convex and taking $\tau_0, \sigma_0 > 0$ such that $\tau_0 \sigma_0 L^2 \leq 1$, where $L^2 = \|\nabla\|^2$ is the squared operator norm, then a forward discretisation of the gradient operator ∇ entails $\|\nabla\|^2 \leq 8$.

The accelerated primal-dual algorithm [9] solving (18) reads:

$$\begin{aligned} \mathbf{y}^{t+1} &= \mathbf{prox}_{\sigma_t \mathcal{H}_\varepsilon^*}(\mathbf{y}^t + \sigma_t \nabla \bar{p}^t) \\ p^{t+1} &= \mathbf{prox}_{\tau_t s}(p^t + \tau_t \operatorname{div} \mathbf{y}^{t+1}) \\ \omega_t &= (1 + 2\hat{\gamma}\tau_t)^{-0.5}, \tau_{t+1} = \omega_t \tau_t, \sigma_{t+1} = \sigma_t / \omega_t \\ \bar{p}^{t+1} &= p^{t+1} + \omega_t (p^{t+1} - p^t), \end{aligned} \quad (19)$$

with proximal maps

$$\begin{aligned} \mathbf{prox}_{\sigma \mathcal{H}_\varepsilon^*}(\mathbf{y}) &= \frac{\mathbf{y}}{1 + \sigma\varepsilon} \left(\max \left\{ 1, \eta^{-1} \left\| \frac{\mathbf{y}}{1 + \sigma\varepsilon} \right\|_{2,\infty} \right\} \right)^{-1}, \\ \mathbf{prox}_{\tau s}(p) &= \left(\frac{1}{\zeta_2^k} + \frac{1}{\tau} \right)^{-1} \left(\frac{v_\diamond^k}{\zeta_2^k} + \frac{p}{\tau} \right). \end{aligned} \quad (20)$$

Algorithm (19) converges to a saddle point (p^*, \mathbf{y}^*) of (18), so we deduce $\mathbf{prox}_{\zeta_2^k \eta \mathcal{H}_\varepsilon}(v_\diamond^k) = p^*$.

¹where we denote by p the minimisation variable instead of v in order to avoid confusion between these inner iterations and the main ones.

Parameters: In the next section we describe different applications to imaging data of Algorithm 1 and test its sensitivity to the weights (η, μ, γ) , with Huberised smoothing of the L^1 gradient norm with fixed smoothing parameter $\varepsilon = 0.05$. For the iPiano algorithm we use the following parameters: the exit condition for the iPiano (with backtracking) scheme is chosen so as to satisfy either the relative error on the energy ($1e-6$) or the maximum number of iterations (10000), with at least few iterations performed so as to assure the inertial contribution; the exit condition for the nested primal-dual problem (19) is set to satisfy either the relative error on the primal-dual gap $1e-4$ or the maximum number of iterations (10000).

V. APPLICATIONS

We apply the model (1) to fuse data from two given images f and b for different applications². The model requests as a further input an α -map $\alpha(\mathbf{x}) \in [0, 1]$ indicating from which of the two images the structural information comes from. In most cases, such map is binary, i.e. $\alpha(\mathbf{x}) \in \{0, 1\}$, so α vanishes on the pixels of the background image b and is equal to one otherwise. Alternatively, α can be smoothed by means of a Gaussian convolution. We rather use the α -matting estimator proposed in [10]. In some cases, we need to align the images f and b , especially for matching the boundaries of the gluing areas where $\alpha \in (0, 1)$. For this reason, we sometimes perform a pre-processing registration step via SIFT features [20]: this is the case for images (g)–(h) but not for (a)–(b) and (d)–(e) since the fusion zone is naturally consistent (e.g. the skin of the faces). We showcase the images f , b and α used in the different experiments presented in Figure 2.

A. Influence of the weights

We are interested in the fusion of two generic images, f and b , shown in images (a)–(c) in Figure 2, via a given α -map. In Figure 3 we show the results from our model for different parameters $\eta \in \{0, 0.1, 0.5\}$, $\nu \in \{10, 100\}$ and $\gamma \in \{0, 1\}$ and for a different starting image u^0 , e.g. $u^0 = f$, u^0 being the α -convex combination of f and b , or their average.

Given the non-convexity of the joint model (1), we notice that the initialisation plays a crucial role in terms of colour preservation. Regarding the parameters, we choose the fidelity parameter μ to be very large with respect to η and γ in order to damp the effect of the regularisation and preserve structural information at every iteration well enough. As expected, the combined effect of the α -map in the fidelity term of u and v as well as the regularisation weight η allows to control the level of the naturalness in information gluing process. Note, for instance, that for an increasing value of η , the staircasing artefact on v due to the TV-type regulariser is more evident. Finally γ controls the amount of the foreground information to be preserved, making its usage relevant for real applications where parts of the image need to remain intact.

²The code is freely available at <https://github.com/simoneparisotto>.

Algorithm 1: Block-coordinate iterative scheme for the joint osmosis model (1)

```

Input      : foreground image  $f$ , background image  $b$ .  $f, b : \Omega \rightarrow [0, 255]$ .  $\alpha$ -map  $\alpha : \Omega \rightarrow [0, 1]$ ;
Output    : the fused image  $u$ ;
Parameters: for the algorithm: tolerance (tol) and maximum number of iterations (maxiter_model); for the model (1): weights  $(\eta, \mu, \gamma)$ ;
              for iPiano:  $\zeta_{1,0}, \zeta_{2,0}, \beta_1, \beta_2, L_{1,0}, L_{2,0} > 0$ , maxiter_iPiano;

Function block_coordinate_osmosis:
   $u^0 = f$  (other choices in Figure 3) and  $v^0 = f^\alpha b^{1-\alpha}$ ; // Initialisation
  for  $k = 0, \dots, \text{maxiter\_model}$  do
    // Compute the explicit iPiano steps
     $u_\diamond^k = u^k - \zeta_{1,k} \partial_u \mathcal{O}(u^k, v^k) + \beta_1 (u^k - u^{k-1})$ ; // with  $\partial_u \mathcal{O}$  as in (14)
     $v_\diamond^k = v^k - \zeta_{2,k} \partial_v \mathcal{O}(u^k, v^k) + \beta_2 (v^k - v^{k-1})$ ; // with  $\partial_v \mathcal{O}$  as in (15)
    // Compute the implicit (proximal) steps of iPiano
    for  $t = 0, \dots, \text{maxiter\_iPiano}$  do
       $p_1 = \text{prox}_{\zeta_{1,k} \gamma \mathcal{D}}(u_\diamond^k)$ ; // computed via (16)
       $p_2 = \text{prox}_{\zeta_{2,k} \eta \mathcal{R}}(v_\diamond^k)$ ; // via the primal-dual Algorithm in (19)
       $\text{gap\_u} = \mathcal{O}(p_1, v^k) - \mathcal{O}(u^k, v^k) - \langle \partial_u \mathcal{O}(u^k, v^k), (p_1 - u^k) \rangle - (L_{1,k}/2) \|p_1 - u^k\|_2^2$ ;
       $\text{gap\_v} = \mathcal{O}(u^k, p_2) - \mathcal{O}(u^k, v^k) - \langle \partial_v \mathcal{O}(u^k, v^k), (p_2 - v^k) \rangle - (L_{2,k}/2) \|p_2 - v^k\|_2^2$ ;
      if  $\text{gap\_u} < 0$  and  $\text{gap\_v} < 0$  then
         $u^{k+1} = p_1$ ;  $v^{k+1} = p_2$ ; // accept and update the variables
        break;
      end
      Update  $\zeta_{1,k}, \zeta_{2,k}, L_{1,k}, L_{2,k}$ ; // according to the standard iPiano rules
    end
    if  $|\mathcal{E}(u^{k+1}, v^{k+1}) - \mathcal{E}(u^k, v^k)| / |\mathcal{E}(u^{k+1}, v^{k+1})| < \text{tol}$  then break; // Exit condition from the main loop
  end
return

```

B. Face fusion

We now focus on a face fusion application. We compare our model with other approaches: the naive direct cloning, the seamless Poisson editing [29], the non-linear fusion [5] (without the pre-processing registration), the classic osmosis filter [33] (with d being the average of the drift associated to f and to b on the transition zone) and our model for which the α -map has been blurred with a Gaussian kernel of standard deviation $\sigma = 5$. In order to compare the different performances, we introduce the *chromaticity error* based on the geometric chromaticity introduced in [14], so as to highlight both the changes in the image structure and in the colour information between the result and the starting image. For a given RGB image z we define $\text{GCM}(z) := \sqrt[3]{z_R \cdot z_G \cdot z_B}$ as the geometric chromaticity mean of z , so that and the pixel-wise chromaticity error between the given u^0 and the output u is

$$\text{error}(u, u^0) = \left| \frac{u_{R,G,B}}{\text{GCM}(u)} - \frac{u_{R,G,B}^0}{\text{GCM}(u^0)} \right|. \quad (21)$$

We report in Figure 4 (zoom in Figure 5) the different approaches used to fuse images in Figure 2 (d) and (e), with (d) as input. The result obtained with our approach is reported in Fig. 4e: it clearly produces a better skin tone than the seamless Poisson editing model, see Fig. 4b, and than the pure osmosis model, see Fig. 4d. The result obtained by the nonlinear fusion model in Fig. 4c is comparable with ours, but from a computational point of view it requires to manually select the eigenvectors to fuse, resulting either into a sharpening effect or undesired results. Furthermore, we note that the chromaticity error map (21) displayed in Figure 5 highlights that the biggest errors are generally localised where image structures change:

our approach mitigates such errors due to the control of the fusion via the blurred α -map and the regularisation on v , see in particular the eyes and the cheeks. This motivates the usage of our approach in the situation where images with similar structure need to be fused, for example for the fusion of multi-modal infrared and visible Cultural Heritage images.

C. Multi-modal fusion in Cultural Heritage

The image in Figure 2g comes from a deluxe copy made in 1290 of *La Somme le roi* by Master Honoré's. This is a "survey for the king" on moral conduct, that consists of five treatises, probably made for Philip IV of France (1285-1314) and his queen, Jeanne of Navarre [30]. The leaf has size 180×125 mm and the miniature 135×90 mm.

The infrared diagnostic at *The Fitzwilliam Museum* (Cambridge, UK) highlighted the presence of a background texture in the gold leaf, damaged throughout centuries, see Figure 2h. In view of fusing the multi-modal images so as to unveil the lost background, we pre-processed the images with a SIFT [20] alignment and computed the α -map via [10]. Then, we apply our model (1) obtaining the result in Figure 6, with zoomed details. As expected from the model, the golden background is well-reconstructed without significantly touching the foreground information.

Figure 2j shows a manuscript from *Biblioteca Capitolare* (Verona, Italy), where the text is highly damaged but still visible with infrared inspection (Figure 2k). We can similarly apply our model (1) with the purpose of text enhancing by means of fusing the structural infrared information with the visible colours of the manuscript. Since multi-modal infrared acquisition can come with noise, we test different regularising

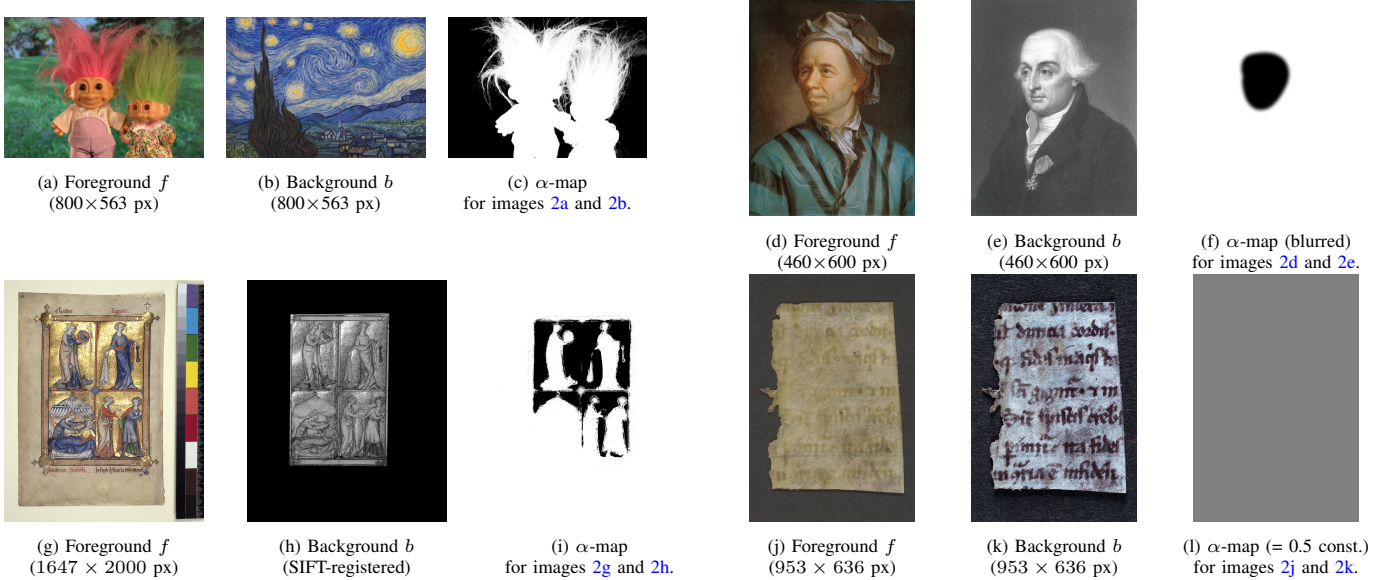


Figure 2: Our dataset for the data fusing applications described in this paper. Fig. 2a from <https://github.com/dingzeyuli/knn-matting>; Fig. 2b *The Starry Night*, by V. Van Gogh, 1889 (CC-PD-Mark 1.0); Fig. 2d: *Portrait of Leonhard Euler (1707-1783)* by J.E. Handmann, Kunstmuseum Basel (CC-PD-Mark 1.0); Fig. 2e *Portrait of Joseph Louis Lagrange* (CC-PD-Mark 1.0); Figs. 2g and 2h: visible (RGB) and infrared images of *La Somme le roi* by Master Honoré’s, MS 368 (by permission of the Syndics of the *Fitzwilliam Museum*, Cambridge, UK); Figs. 2j and 2k: visible (RGB) and infrared images of a manuscript with text (courtesy of *Biblioteca Capitolare*, Verona, Italy); Figs. 2c, 2f, 2i and 2l: α -maps.

parameter η for an heuristically fixed choice of μ and γ . In Figure 7, we report different results showing that the larger η is, the more the typical staircasing effect is visible in the fusion of the structural information. This effect, is desirable in this application for enhancing the edges of the letters.

We remark that despite the availability of few metrics assessing the quality of image fusion based either on image correlation [4] or on deep learning [19], we remark that for Cultural Heritage applications the validation of the optimal result is performed by expert users, so as to take into account not only image features, but possible other characteristics such as author style, historic period, illumination, etc.

VI. CONCLUSIONS

In this work we introduced a new model for nonlinear image fusion. The fusion process is driven by an *osmosis* term and involves also a regularisation term and a fidelity term on the data. After motivating the model from a theoretical point of view, we discussed its numerical implementation and we applied it to solve different problems in the context of data fusion. In particular, we highlighted the potentialities of the model for applications in Cultural Heritage imaging, from the unveiling of missed structures to text enhancing.

As future directions, we envisage the use of structural information not only in the drift field but also to build an anisotropy metric in the model, e.g. via the directional osmosis energy of [27]. The fusion could also be performed with the same model in the spectral domain. At the same time, it could be of interest to force the regulariser to act only onto one of the two images to be fused, i.e. assuming that one image comes with noise and the other is noise-free.

Future work shall possibly investigate the combination of our model with modern deep learning approaches which have recently become increasingly popular to solve the image fusion problem, see [19] for a review.

ACKNOWLEDGMENT

The authors thank Prof. Joachim Weickert for fruitful discussions related to this work. SP acknowledges the Leverhulme Trust project on “Unveiling the invisible: mathematics for conservation in arts and humanities”. LC acknowledges the support given by the Fondation Mathématique Jacques Hadamard (FMJH). The CH diagnostics were supported by Dr Stella Panayotova and Dr Paola Ricciardi for Fig. 2h (Fitzwilliam Museum, Univ. of Cambridge), Dr Claudia Daffara (Univ. of Verona) for Fig. 2k. CBS acknowledges support from the Leverhulme Trust project on Breaking the non-convexity barrier, the Philip Leverhulme Prize, the EPSRC grant No. EP/M00483X/1, the EPSRC Centre No. EP/N014588/1, the European Union Horizon 2020 research and innovation programmes under the Marie Skłodowska-Curie grant agreement No. 691070 CHiPS, the Cantab Capital Institute for the Mathematics of Information and the Alan Turing Institute. This project has also received funding from the European Union’s Horizon 2020 research and innovation programme NoMADS under the Marie Skłodowska-Curie grant agreement No 777826.

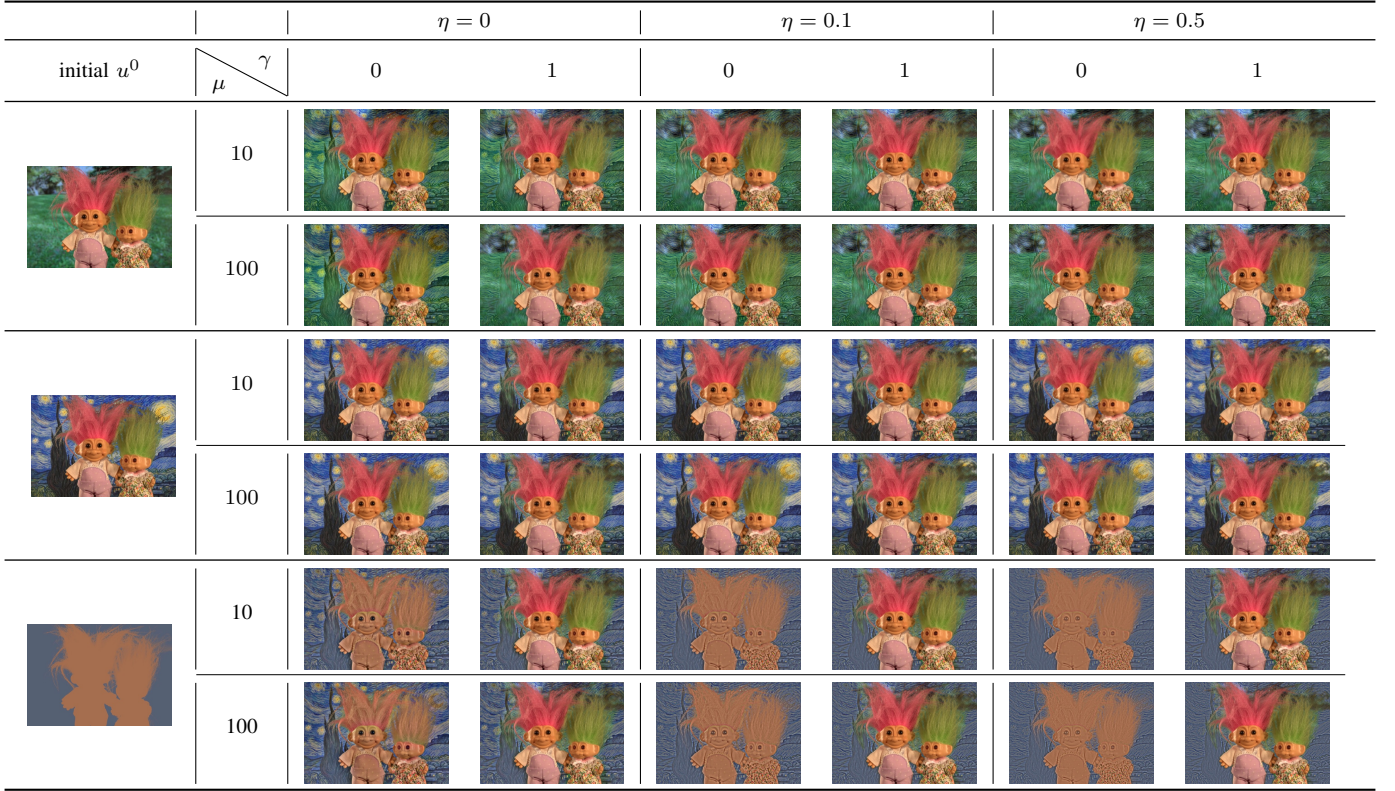


Figure 3: Effect of different weighting parameters and initialisation for (1) and images 2a-2b.



Figure 4: Comparison of different face fusion approaches.

APPENDIX

We detail here the derivation of (15):

$$\begin{aligned} \frac{\partial}{\partial v} \left(\int_{\Omega} v \left| \nabla \left(\frac{u}{v} \right) \right|^2 d\mathbf{x} \right) &= \frac{\partial}{\partial v} \int_{\Omega} v \frac{v \nabla u - u \nabla v}{v^2} \cdot \frac{v \nabla u - u \nabla v}{v^2} d\mathbf{x} \\ &= \underbrace{\frac{\partial}{\partial v} \int_{\Omega} \frac{\nabla u \cdot \nabla u}{v} d\mathbf{x}}_{(a)} - \underbrace{\frac{\partial}{\partial v} \int_{\Omega} \frac{2u \nabla u \cdot \nabla v}{v^2} d\mathbf{x}}_{(b)} + \underbrace{\frac{\partial}{\partial v} \int_{\Omega} \frac{u^2 \nabla v \cdot \nabla v}{v^3} d\mathbf{x}}_{(c)}. \end{aligned}$$

By splitting the computations into (a), (b) and (c), we have:

$$(a) = \frac{\partial}{\partial v} \int_{\Omega} \frac{\nabla u \cdot \nabla u}{v} d\mathbf{x} = \int_{\Omega} -\frac{\nabla u \cdot \nabla u}{v^2} d\mathbf{x};$$

$$\begin{aligned} (b) &= \frac{\partial}{\partial v} \int_{\Omega} \frac{2u}{v^2} \nabla u \cdot \nabla v d\mathbf{x} \\ &= \int_{\Omega} \frac{\partial}{\partial v} \left(\frac{2u}{v^2} \right) \nabla u \cdot \nabla v + \frac{2u}{v^2} \frac{\partial}{\partial v} (\nabla u \cdot \nabla v) d\mathbf{x} \\ &= \int_{\Omega} \frac{\partial}{\partial v} \left(\frac{2u}{v^2} \right) \nabla u \cdot \nabla v + \frac{2u}{v^2} \nabla u \cdot \nabla \mathbf{I} d\mathbf{x} \\ &= \int_{\Omega} -\frac{4u}{v^3} \nabla u \cdot \nabla v - \text{div} \left(\frac{2u}{v^2} \nabla u \right) d\mathbf{x}; \\ (c) &= \frac{\partial}{\partial v} \int_{\Omega} \frac{u^2}{v^3} \nabla v \cdot \nabla v d\mathbf{x} \\ &= \int_{\Omega} \frac{\partial}{\partial v} \left(\frac{u^2}{v^3} \right) \nabla v \cdot \nabla v + \frac{u^2}{v^3} \frac{\partial}{\partial v} (\nabla v \cdot \nabla v) d\mathbf{x} \\ &= \int_{\Omega} -3 \frac{u^2}{v^4} \nabla v \cdot \nabla v + \frac{u^2}{v^3} \nabla v \cdot \nabla \mathbf{I} d\mathbf{x} \\ &= \int_{\Omega} -3 \frac{u^2}{v^4} \nabla v \cdot \nabla v - v \text{div} \left(\frac{u^2}{v^3} \nabla v \right) d\mathbf{x}. \end{aligned}$$

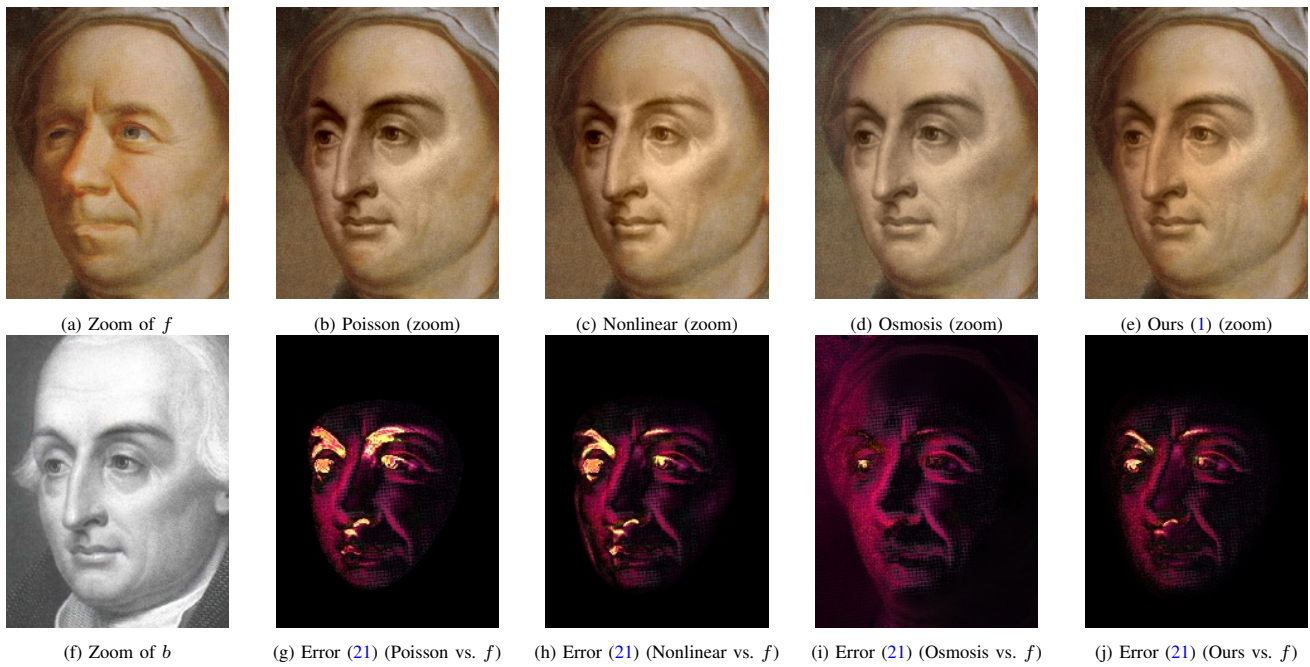


Figure 5: Zoom of face fusion results from Figure 4 and chromaticity error (21).

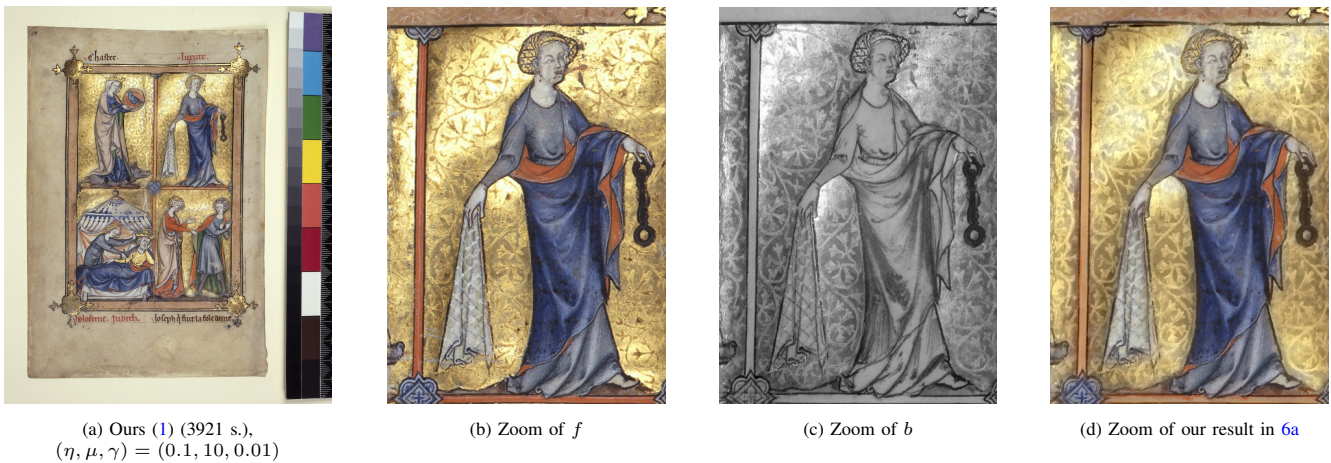


Figure 6: Application to Cultural Heritage Images. Initialisation $u^0 = f$.



Figure 7: Text enhancing from a manuscript.

REFERENCES

- [1] K. Amolins, Y. Zhang, and P. Dare, "Wavelet based image fusion techniques - an introduction, review and comparison," *ISPRS J. of Photogrammetry and Rem. Sensing*, vol. 62, no. 4, pp. 249 – 263, 2007.
- [2] C. Ancuti, C. O. Ancuti, C. De Vleeschouwer, and A. C. Bovik, "Night-time dehazing by fusion," in *IEEE ICIP*, 2016, pp. 2256–2260.
- [3] C. Ancuti, C. O. Ancuti, T. Haber, and P. Bekaert, "Enhancing underwater images and videos by fusion," in *IEEE CVPR*, 2012, pp. 81–88.
- [4] V. Aslantas and E. Bendes, "A new image quality metric for image fusion: The sum of the correlations of differences," *AEU - Int. J. Electron. C.*, vol. 69, no. 12, pp. 1890–1896, 2015.
- [5] M. Benning, M. Möller, R. Z. Nossek, M. Burger, D. Cremers, G. Gilboa, and C.-B. Schönlieb, "Nonlinear spectral image fusion," in *SSVM*, 2017, pp. 41–53.
- [6] P. J. Burt and E. H. Adelson, "A multiresolution spline with application to image mosaics," *ACM Trans. Graph.*, vol. 2, no. 4, pp. 217–236, 1983.
- [7] L. Calatroni, C. Estatico, N. Garibaldi, and S. Parisotto, "Alternating Direction Implicit (ADI) schemes for a PDE-based image osmosis model," *J. Phys. Conf. Ser.*, vol. 904, no. 1, p. 012014, 2017.

- [8] L. Calatroni, M. d’Autume, R. Hocking, S. Panayotova, S. Parisotto, P. Ricciardi, and C.-B. Schönlieb, “Unveiling the invisible: mathematical methods for restoring and interpreting illuminated manuscripts,” *Heritage Science*, vol. 6, no. 1, p. 56, 2018.
- [9] A. Chambolle and T. Pock, “A first-order primal-dual algorithm for convex problems with applications to imaging,” *J. Math. Imaging Vision*, vol. 40, no. 1, pp. 120–145, 2011.
- [10] Q. Chen, D. Li, and C.-K. Tang, “Knn matting,” *IEEE Trans. Pattern Anal. Mach. Intell.*, vol. 35, no. 9, pp. 2175–2188, 2013.
- [11] M. d’Autume, J. Morel, and E. Meinhardt-Llopis, “A flexible solution to the osmosis equation for seamless cloning and shadow removal,” in *IEEE ICIP*, 2018, pp. 2147–2151.
- [12] R. Fattal, D. Lischinski, and M. Werman, “Gradient domain high dynamic range compression,” in *ACM Trans. Graph.*, vol. 21, no. 3, 2002, pp. 249–256.
- [13] J. Fehrenbach and J.-M. Mirebeau, “Sparse non-negative stencils for anisotropic diffusion,” *J. Math. Imaging Vision*, vol. 49, no. 1, pp. 123–147, 2014.
- [14] G. D. Finlayson, S. D. Hordley, Cheng Lu, and M. S. Drew, “On the removal of shadows from images,” *IEEE Trans. Pattern Anal. Mach. Intell.*, vol. 28, no. 1, pp. 59–68, 2006.
- [15] K. Hagenburg, M. Breuß, J. Weickert, and O. Vogel, “Novel schemes for hyperbolic pdes using osmosis filters from visual computing,” in *SSVM*, 2011, pp. 532–543.
- [16] A. P. James and B. V. Dasarathy, “Medical image fusion: A survey of the state of the art,” *Inform. Fusion*, vol. 19, pp. 4–19, 2014.
- [17] S. Li, X. Kang, L. Fang, J. Hu, and H. Yin, “Pixel-level image fusion: A survey of the state of the art,” *Inform. Fusion*, vol. 33, pp. 100–112, 2017.
- [18] S. Li and B. Yang, “Multifocus image fusion by combining curvelet and wavelet transform,” *Pat. Recogn. Lett.*, vol. 29, no. 9, pp. 1295–1301, 2008.
- [19] Y. Liu, X. Chen, Z. Wang, Z. J. Wang, R. K. Ward, and X. Wang, “Deep learning for pixel-level image fusion: Recent advances and future prospects,” *Inform. Fusion*, vol. 42, pp. 158–173, 2018.
- [20] D. G. Lowe, “Object recognition from local scale-invariant features,” in *IEEE ICCV*, vol. 2, 1999, pp. 1150–1157.
- [21] J. Ma, Y. Ma, and C. Li, “Infrared and visible image fusion methods and applications: A survey,” *Inform. Fusion*, vol. 45, pp. 153–178, 2019.
- [22] T. Mertens, J. Kautz, and F. Van Reeth, “Exposure fusion,” in *Proc. Pac. Conf. Comput. Graph. Appl.*, 2007, pp. 382–390.
- [23] D. Mishra and B. Palkar, “Image fusion techniques: a review,” *Int. Journal of Computer Applications*, vol. 130, no. 9, pp. 7–13, 2015.
- [24] R. Moreno, L. Pizarro, B. Burgeth, J. Weickert, M. A. Garcia, and D. Puig, “Adaptation of tensor voting to image structure estimation,” in *New Developments in the Visualization and Processing of Tensor Fields*, 2012, pp. 29–50.
- [25] P. Ochs, Y. Chen, T. Brox, and T. Pock, “iPiano: Inertial proximal algorithm for nonconvex optimization,” *SIAM J. Imaging Sci.*, vol. 7, no. 2, pp. 1388–1419, 2014.
- [26] G. Pajares and J. M. de la Cruz, “A wavelet-based image fusion tutorial,” *Pat. Recogn.*, vol. 37, no. 9, pp. 1855 – 1872, 2004.
- [27] S. Parisotto, L. Calatroni, M. Caliari, C.-B. Schönlieb, and J. Weickert, “Anisotropic osmosis filtering for shadow removal in images,” *Inverse Problems*, vol. 35, no. 5, p. 054001, 2019.
- [28] S. Parisotto, L. Calatroni, and C. Daffara, “Digital cultural heritage imaging via osmosis filtering,” in *ICISP 2018*, 2018, pp. 407–415.
- [29] P. Pérez, M. Gangnet, and A. Blake, “Poisson image editing,” *ACM Trans. Graph.*, vol. 22, no. 3, pp. 313–318, 2003.
- [30] R. H. Rouse and M. A. Rouse, *Manuscripts and their makers: commercial book producers in medieval Paris, 1200-1500*. Turnhout: Harvey Miller, 2000.
- [31] J. Thies, M. Zollhöfer, M. Nießner, L. Valgaerts, M. Stamminger, and C. Theobalt, “Real-time expression transfer for facial reenactment,” *ACM Trans. Graph.*, vol. 34, no. 6, pp. 183–1, 2015.
- [32] O. Vogel, K. Hagenburg, J. Weickert, and S. Setzer, “A fully discrete theory for linear osmosis filtering,” in *SSVM*, 2013, pp. 368–379.
- [33] J. Weickert, K. Hagenburg, M. Breuß, and O. Vogel, “Linear osmosis models for visual computing,” in *EMMCVPR*, 2013, pp. 26–39.



Simone Parisotto received the Ph.D. degree in Applied Mathematics at the University of Cambridge (UK) in 2019. Before that, he received the B.Sc. and the M.Sc. in Mathematics at the University of Verona (Italy). He is currently a Post-Doc at the University of Cambridge, in the Cambridge Image Analysis group and the Fitzwilliam Museum, working on mathematical applications for Cultural Heritage. His research interests focus also on variational and numerical methods for inverse imaging problems.



Luca Calatroni completed his Ph.D. in Applied Mathematics in 2015 as part of the Cambridge Image Analysis research group (UK). After that, he carried out his post-doctoral research activity at the University of Genova (Italy) and at the École Polytechnique (France) as a *Lecteur Hadamard* fellow funded by the FMJH. From October 2019, he is a full time CNRS researcher at the I3S laboratory in Sophia Antipolis, France. His research focuses on variational methods and non-smooth optimisation algorithms for imaging.



Aurélien Bugeau received the Ph.D. degree in signal processing from the University of Rennes, France, in 2007. She is currently an Associate Professor with the University of Bordeaux and with the Laboratoire Bordelais de Recherche en Informatique, where she is involved in research. Her main research interests include patch-based and deep-learning-based methods for image, video and point cloud processing and analysis.



Nicolas Papadakis received a M. Eng. degree in applied mathematics from the National Institute of Applied Sciences, Rouen, France (2004), a M. Sc in Analysis from University of Rouen (2004) and the Ph.D. degree in applied mathematics from the University of Rennes, France (2007). He is currently a full time CNRS Researcher at Institut de Mathématiques de Bordeaux, France. His research focuses on variational methods and optimal transportation for image processing applications.



Carola-Bibiane Schönlieb received her PhD degree in Mathematics from the University of Cambridge in 2009. After one year of postdoctoral activity at the University of Göttingen (Germany), she became a Lecturer at the University of Cambridge in 2010, promoted to Reader in 2015 and promoted to Professor in 2018. Her research interests focus on variational methods, partial differential equations and machine learning for image analysis, image processing and inverse imaging problems.